Spruce Hard Carbon Anodes for Lithium-Ion Batteries

Mathias Drews,[a] Jan Büttner,[b, c, d] Manuel Bauer,[a] Junaid Ahmed,[a] Rajib Sahu,[e, f] Christina Scheu,[e, f] Severin Vierrath,*[c, g] Anna Fischer,*[b, c, d, h] and Daniel Biro*[a]

In this work, lithium-ion battery full-cells based on spruce-derived hard carbon anodes and an electrochemical pre-lithiation method are presented in combination with a detailed analysis of full-cell operation and the lithiation state. The physical and electrochemical properties agree well with those of previous biomass-derived hard carbon anodes. However, low initial coulombic efficiencies of 65% represent one of the major challenges of the developed anodes with respect to full-cell operation. To counteract the initial lithium loss, in-situ electro-chemical pre-lithiation was conducted, allowing battery operation in the same cell setup without reassembly. Consequently, significantly increased capacities, cycle life, and first cycle coulombic efficiency were obtained in comparison to untreated anodes (195 mAh/g versus 150 mAh/g, state of health (SOH) 80 after 150 cycles versus 70 cycles, and 90% versus 65%). In summary, spruce-based hard carbon has the potential to be an environmentally friendly alternative to standard graphite.

1. Introduction

Due to the strongly increasing demand for lithium-ion batteries (LIBs), it is suspected that the supply of several materials could become critical in the near future.[1] For the negative electrode

[a] M. Drews, M. Bauer, J. Ahmed, Dr. D. Biro
     Fraunhofer Institute for Solar Energy Systems, ISE
     Heidenhofstraße 2, 79110 Freiburg, Germany
     E-mail: daniel.biro@ise.fraunhofer.de
[b] J. Büttner, Prof. A. Fischer
     Institute for Inorganic and Analytical Chemistry
     University of Freiburg
     Albertstraße 21, 79104 Freiburg, Germany
     E-mail: anna.fischer@ac.uni-freiburg.de
[c] J. Büttner, Dr. S. Vierrath, Prof. A. Fischer
     Freiburg Center for Interactive Materials and Bioinspired Technologies, FIT
     University of Freiburg
     Georges-Köhler-Allee 105, 79110 Freiburg, Germany
[d] J. Büttner, Prof. A. Fischer
     Cluster of Excellence livMatS
     University of Freiburg
     79104 Freiburg, Germany
[e] Dr. R. Sahu, Prof. C. Scheu
     Max Planck Institute for Iron Research
     Max-Planck-Straße 1, 40237 Düsseldorf, Germany
[f] Dr. R. Sahu, Prof. C. Scheu
     Materials Analytics
     RWTH University of Aachen
     Kopernikusstraße 10, 52074 Aachen, Germany
[g] Dr. S. Vierrath
     Electrochemical Energy Systems, IMTEK - Department of Microsystems Engineering
     University of Freiburg
     Georges-Köhler-Allee 103, 79110 Freiburg, Germany
[h] Prof. A. Fischer
     Freiburg Materials Research Center, FMF
     University of Freiburg
     Stefan-Meier-Straße 21, 79104 Freiburg, Germany

     Supporting information for this article is available on the WWW under https://doi.org/10.1002/celc.202101174

of LIBs, graphite is typically used, which is either mined as "natural graphite" or produced as "synthetic graphite" from oil refining by-products.[2] Due to limited reserves, mostly located in China, the European Union and the United Stated have classified natural graphite as critical raw material.[1,3] Furthermore, the mining of graphite resources is often accompanied by negative impacts on the environment and population.[4] Synthetic graphite is usually synthesized at temperatures above 2500°C and leads to the emission of greenhouse gases or pollutants such as CO_2, NO_x, SO_x and CO, resulting in a relatively high carbon footprint of the corresponding anode material.[5] Thus, alternative anode materials based on renewable raw materials are attracting great interest. A very promising candidate to replace the standard graphite anode thereby is hard carbon, obtained by pyrolysis of biomass. Corresponding anode materials would therefore not only preserve fossil resources, but also would act as a carbon sink.

Hard carbon stands out as a non-graphitizable material.[6,7] With respect to electrochemical properties, hard carbon anodes show capacities comparable to and even higher than those of graphite. However, the application of hard carbon anodes in commercial LIBs is critical because their open pores and organic functionalities on the surface lead to low efficiencies, especially in the first cycle.[8–10] Furthermore, the storage mechanism of metal ions in hard carbon is not clarified yet in full detail. For instance, early studies by Stevens and Dahn[11] propose an "intercalation-adsorption" mechanism for sodium and lithium storage while alternative work suggests a "adsorption-intercalation" process.[12,13] Furthermore, a familiar study on the storage mechanism of sodium ions in hard carbon shows a capacity of 333.4 mAh/g according to a chemical formulation of $NaC_{6.7}$.[14] Besides commercially available hard carbons,[15,16] hard carbon anodes from various renewable raw materials have been intensively studied in LIBs and sodium ion batteries, e.g., from pine cones,[17] leaves,[18] reed catkins,[19] rice husk,[20,21] nut shells,[22] mushrooms,[23,24] banana peels,[25] corn cobs[26], orange peels,[27] avocado seeds,[28] apple waste,[29] tamarind fruits,[30] synthetic waste[31,32] and wood precursors[10,33,34], but also from

ChemElectroChem

Articles
doi.org/10.1002/celc.202101174

Chemistry Europe
European Chemical
Societies Publishing

animal residues such as prawn shells[35] and ox horn,[36] and even from human hair.[37] Although batteries based on such materials principally show very promising electrochemical properties, the majority of articles remain at the half-cell level. For instance, Jianyong et al. demonstrated a capacity of 210 mAh/g and a cycling potential of 3.000 cycles for orange peel-derived hard carbons in lithium-ion half-cells. However, the first cycle efficiency of less than 50% indicates limited applicability in practical LIBs.[27] Similarly, Li et al. presented porous carbon anode materials derived from rice husk lignin with capacities of around 470 mAh/g after 100 cycles and a coulombic efficiency of less than 50% in the first cycle.[21] Thus, material or process modifications are needed to make biomass-derived hard carbon materials usable for lithium-ion full-cells.

In this regard, Xing et al. published properties of hard carbon anodes synthesized from glucose at different pyrolysis temperatures. With increasing temperature, the surface area and initial lithium losses of the material decreased. The reason for this trend was thought to be the closing of open pores in the material and a direct proportionality was found between surface area and initial lithium losses.[7,9] Tenhaeff et al. presented hard carbon anodes derived from lignin precursors synthesized at 1000 °C, 1500 °C and 2000 °C.[10] Between 1000 °C and 1500 °C, they observed a dramatic decrease of the initial losses, which they correlated to insufficient elimination of organic/surface functionalities at lower temperatures. Although comparable efficiencies with graphite were achieved, no results were presented for full-cells.

In addition to the possibility to reduce initial losses by increasing the process temperature, another important mitigation strategy is the so-called "pre-lithiation".[38] The basic concept of pre-lithiation is to build up the solid electrolyte interphase (SEI) layer of the anode before full-cell assembly and to add extra lithium to the full-cell to compensate initial capacity losses. Prominent examples of pre-lithiation methods are direct contact between lithium and the anode,[32,39] electrochemical[29,40,41] and/or chemical pre-lithiation.[15,42] Regarding the first, stabilized lithium metal powder (slmp) is one of the most prominent representatives.[43] However, slmp is relatively expensive and can lead to an inhomogeneous distribution of lithium on the surface of the anode. With respect to chemical pre-lithiation, Zhang et al. recently published the pre-lithiation of a commercial hard carbon material using lithium biphenylide dissolved in tetrahydrofuran. The group demonstrated a significant increase in initial coulombic efficiencies by this pre-lithiation method (from 75.5% to 90.2%) as well as full-cell performance with lithium nickel manganese cobalt oxide (NMC (111)) at the cathode.[15] High reactivity, however, of pre-lithiation agents can entail enormous safety concerns

especially in large-scale production. Wu et al. used apple waste as a carbon precursor to synthesize hard carbon anodes for sodium-ion batteries at 1100 °C. The pre-sodiation was based on an electrochemical method where the anode was sodiated to 0.02 V vs. Na/Na$^+$ in a coin cell before the full-cell assembly. The corresponding 3-electrode full-cell showed a capacity of 250 mAh/g$_{anode}$ and 80% of its initial capacity (SOH80) after 100 cycles at 0.1 °C. The cell also showed considerable rate performance up to a current rate of 2 °C.[29] Regardless of pre-lithiation, lithium-ion full-cells based on biomass-derived hard carbons are sparsely represented.[34,44] For instance, Nowak et al. demonstrated lignin-based carbon fibers from pine and spruce as precursor for hard carbon anodes.[34] However, only limited full-cell performance over 22 cycles was obtained in combination with a relatively low first cycle coulombic efficiency (around 75%). As an outlook, the group proposed pre-lithiation as a possible strategy to improve cell performance.

In summary, numerous examples of the use of renewable materials as promising carbonaceous anodes for lithium-ion batteries can be found in the literature. However, corresponding full-cells as the next step towards a future commercialization have rarely been presented. Thus, in this work, we focus on the construction of biomass-derived hard carbon lithium-ion full-cells with improved capacity and cycle life in combination with a detailed investigation of battery operation. The hard carbon anode materials are synthesized from spruce wood and electrochemically pre-lithiated in a full-cell, allowing subsequent cycling and characterization without reassembly.

2. Results and Discussion

2.1. Synthesis of Hard Carbon from Spruce Wood

The synthesis of the spruce-derived hard carbon followed an adapted protocol reported by Wu et al.,[29] using a different biomass feedstock. Similar to recent studies, the production of hard carbon mainly consisted of dehydration followed by pyrolysis of spruce wood.[45,46] A scheme of the synthesis route is shown in Figure 1. After dehydration of the wood and sawdust by simple water evaporation, the remaining moisture was removed by adding phosphoric acid to the sawdust. In addition to the drying property, phosphoric acid is known to act as an activation agent, leading to high porosity and surface area.[47] After pyrolysis of the aged sawdust-acid mixture at 1100 °C, 39 wt% of the sawdust remained as hard carbon material. The bulk elemental distribution of the spruce-derived hard carbon was measured by CHNS analysis yielding 94 wt% carbon, 1 wt% hydrogen, and 1 wt% nitrogen (4 wt% residual). No sulfur was
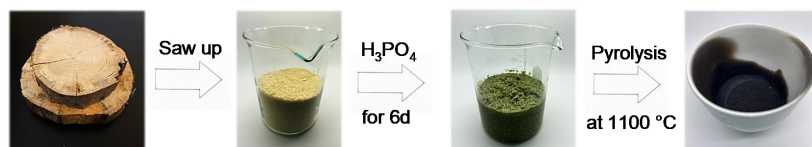

Saw up → H$_3$PO$_4$ for 6d → Pyrolysis at 1100 °C

Figure 1. Diagram of spruce hard carbon synthesis.

ChemElectroChem

Articles
doi.org/10.1002/celc.202101174

Chemistry
Europe
European Chemical
Societies Publishing

found in the hard carbon, and the residual is suggested to consist mainly of oxygen and potentially some phosphorus (from the phosphoric acid treatment).

2.2. Physicochemical Properties of the Spruce Hard Carbon

The physicochemical properties of the spruce hard carbon were investigated using X-ray diffraction (XRD), Raman spectroscopy, scanning electron microscopy (SEM), high resolution transmission electron microscopy (HRTEM), energy-dispersive X-ray spectroscopy (EDX), X-ray photoelectron spectroscopy (XPS), and nitrogen physisorption. Figure 2a shows typical XRD reflections (copper source, $\lambda = 1.54$ Å) found for hard carbons,[29,45,46] with (002), (101), and (110) reflections found at 2θ values of 22.3°, 43.7°, and 79.5°. Based on Bragg's equation, an interlayer spacing d_{002} of 0.4 nm was found, which is consistent with comparable hard carbons[13,48,49,49] but larger compared to the interlayer spacing of graphite ($d_{002} = 0.34$ nm)[13]. The Raman spectrum (see Figure 2b) shows the characteristic D1 and G bands at around 1344 cm^{-1} and around 1580 cm^{-1}, which is in good agreement with former studies on biomass-based hard carbons.[21,46] The ratio between the integrated intensity of the D1 and G bands (A_{D1}/A_G), which indicates the degree of graphitization, was determined to be around 3.3. Similar but slightly lower values were recently published for hard carbon derived from a commercial lignin source pyrolyzed at 1200°C, suggesting a lower degree of graphitization of the hard carbon synthesized in our work.[50] However, it is very difficult to use such findings (based on XRD and Raman) to explain differences between cell performances since there are several other differences influencing electrochemistry (e.-g., particle size distribution and chemical pretreatments of the active material, weight ratios of active material and binder, electrode porosity, binder distribution in the electrode, cycling parameters - especially electrochemical conditioning, and differences between sodium and lithium-ion batteries). For the detailed deconvolution of the Raman signal with a graphitic and 4 defect bands see Figure S1.[51] On the SEM image (Figure 2c) of the spruce hard carbon powder, a relatively wide
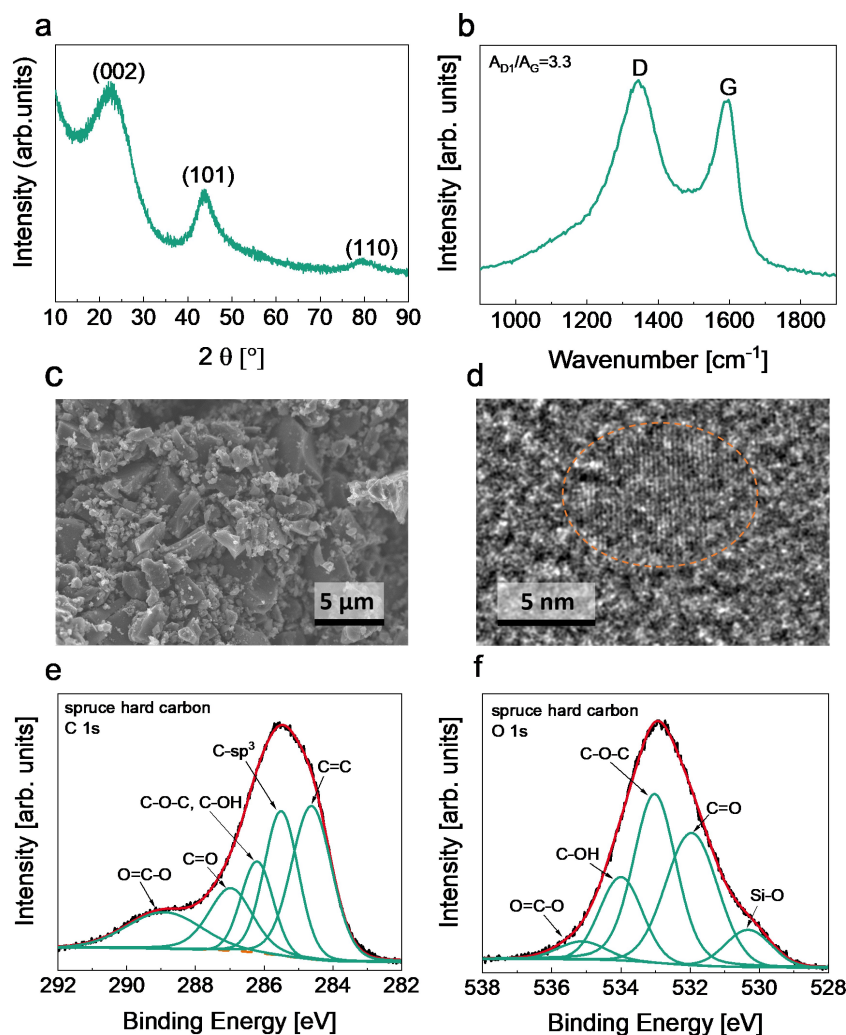

Figure 2. a) XRD pattern, b) Raman spectrum, c) SEM image (magnification 5000×), d) HRTEM image (crystalline domains inside orange circle), e) XPS C 1s core level and f) XPS O 1s core level spectrum (background is illustrated as an orange scattered line) of spruce hard carbon.

distribution of particle sizes can be observed, ranging from hundreds of nanometers to several micrometers. A similar particle size distribution was found for a hard carbon anode from apple waste.[29] However, the particle sizes do not seem to exceed 10 μm significantly. Thus, the maximum particle size is obviously smaller compared to the technical feasible maximum of 54 μm (separation of the particles with a sieve with 54 μm mesh size, see experimental section). For a better overview, a SEM image with a magnification of 1500x and 50000x is shown in supporting information Figure S2. Especially from the higher magnification (see inset in Figure S2), a rough surface of the hard carbon particles can be seen rather than distinct holes. However, physisorption measurements were performed (further on in this section) to investigate the porosity in detail. EDX spectroscopy detected 93.3 wt% carbon, 4.1 wt% oxygen, and 1.6 wt% phosphorus (see spectrum in Figure S3 and Table S1 in the supporting information), where the phosphorus fraction likely originated from the phosphoric acid pretreatment (see experimental section). This result is in good agreement with elemental analysis. However, the carbon fraction must be treated with care because the powder was mounted on a carbon-containing glue. Thus, part of the carbon signal may originate from the glue, although care was taken to measure the sample at a relatively high powder accumulation and with a moderate acceleration voltage. To better understand the hard carbon microstructure, HRTEM images (Figure 2d) of the spruce hard carbon sample are presented. Besides amorphous regions, crystalline domains (highlighted in orange) are clearly visible. Furthermore, a lattice spacing of around 2.1 Å was found for the crystalline domain, which agrees well with the d_{101} spacing found in the XRD pattern (2.07 Å, determined by Bragg's equation). The HRTEM images confirm the semi-crystalline character suggested by Raman and XRD measurements (for a better overview, further HRTEM images are given in the supporting information Figure S4).

X-ray photoelectron spectroscopy was applied to investigate the surface elemental distribution of spruce hard carbon and the associated binding species. The XPS survey spectrum is given in the supporting information (Figure S5). Figure 2e shows the C 1s core level spectrum. The spectrum can be deconvoluted with five signals at 284.6 eV, 285.5 eV, 286.2 eV, 287.0 eV and 288.9 eV, possibly corresponding to C=C (C-sp^2), C-sp^3, C—O—C (ether) and C—OH (alcohol), C=O (carbonyl) and O=C-O (carboxyl) containing species.[52] The C-sp^3 peak is assumed to contain the C—C and C—H features. However, the signals are too close together to be deconvoluted at the given resolution[46]. The O 1s core level spectrum can be seen in Figure 2f. Four carbonaceous oxygen features at 532.0 eV, 533.0 eV, 534.0 eV and 535.1 eV were used to deconvolute the signal. Possible assignments are C=O, C—O—C, C—OH and O=C—O species.[53] Since the deconvolution of the O 1s core level spectrum is divergent in the literature, the assignments given here represent only one possibility. Due to possible silicon contamination during the production process, the signal at 530.3 eV can be assigned to a Si—O species. Further signals (i.e., the Si 2s and the Si 2p) that support the detection of silicon can be seen in the survey spectrum (Figure S5). From the

integrated intensities of the C 1s and the O 1s core level spectra, an oxygen/carbon ratio of approximately 0.4 (at%/at%) was found (71 at% carbon and 29 at% oxygen, 65 wt% carbon and 35 wt% oxygen). Combined evaluation of the C 1s and the O 1s core level spectra produced self-consistently the following possible assignments of oxygen-containing functional groups: Carbonyl (35.5 at%), ester (26.7 at%), alcohol (18.5 at%), ether (14.9 at%), and carboxyl (4.4 at%). The oxygen functionalization is in good qualitative agreement with the EDX mapping results, suggesting a homogeneous oxygen distribution over the whole electrode surface (see Figure 3c). Although surface functional groups support SEI growth, they are also suggested to improve electrochemical performance as they can act as lithium insertion sites.[35] The ratio between C-sp^2 (C=C) and C-sp^3 is 1.3. However, it needs to be mentioned that this value is only true for the surface of the material.

In comparison with elemental analysis, revealing the bulk composition of the sample, the oxygen/carbon ratio determined by XPS is rather high. However, the surface sensitivity of XPS needs to be considered. Thus, it can be deduced that mostly the first outer nanometers of the hard carbon are oxygen rich. In addition, the ratio of oxygen to carbon is high compared to the literature, suggesting relatively high oxidation and functionalization of the spruce hard carbon surface.[46] According to literature, higher temperatures could reduce the amount of functionalities.[10] However, increased temperatures entail higher energy demands, and the scope of this work is to demonstrate a simple synthesis that includes a pre-lithiation approach to compensate for the initial losses due to SEI formation.

Physisorption measurements are key to measure the porous structure of carbons since pore size, pore distribution and surface area of the carbon used in the anode are crucial factors influencing the electrochemical performance of LIBs. The nitrogen adsorption-desorption isotherm can be seen in Figure S6a. The DFT pore size distribution (see Figure S6b) shows the existence of unresolved micropores with diameters of
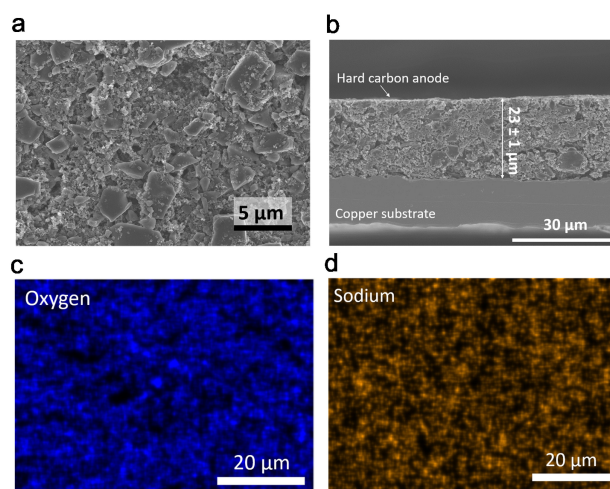

Figure 3. SEM image of spruce hard carbon anode in a) top view (magnification 5 000 x), b) cross section (magnification 1 500×), c) oxygen and d) sodium top view EDX mapping

ChemElectroChem

Articles
doi.org/10.1002/celc.202101174

**Chemistry
Europe**

European Chemical
Societies Publishing

< 0.89 nm (27.9 vol%) and micropores with diameters between 0.89 nm and 2 nm (13.7 vol%), small mesopores with diameters between 2 nm and 4 nm (6.9 vol%), and a broad distribution of larger mesopores (51.5 vol%). The BET surface area was calculated to be 61 m^2/g, which is comparable to recently published lignin-based hard carbons.[46]

SEM images and EDX measurements of the anode surface and cross-section were performed for a closer examination of the morphology and elemental distribution of the spruce hard carbon anode. Figure 3a shows the top view of a spruce hard carbon anode. In comparison to the pristine powder (see Figure 2c), the particle morphology and distribution are largely maintained. Larger spruce hard carbon particles are embedded in small micro- and nano-hard carbon and carbon black particles. From the SEM image, it can be concluded that the processing (i.e., mixing and three-roll milling) leads to a very homogeneous distribution of the particles. Similarly, the SEM image of the cross-section reveals a similar particle size distribution and an even processing. After drying the anode, a coating thickness of approximately 23 µm was reached.

The elemental distribution measured by SEM EDX (in top view) was very similar to the pristine powder (see Figure S7 and Table S2). However, similar to the evaluation of the pristine powder, the carbon signal might be influenced by the signal from the carbon glue where the electrode is mounted. Approximately 1 wt% of sodium was found in the electrode, which most likely stems from the Na-CMC binder. The oxygen and sodium mapping (Figure 3c and d) suggests a homogeneous binder distribution, whereby the oxygen originates not only from the binder but also from the surface functionalization. Elemental distribution of a spruce hard carbon anode in cross section is similar to the top view investigation (see Figure S8

and Table S3). For the analysis of the elemental composition of the cross section, only a specific area (see Figure S9) of the hard carbon anode, excluding the copper current collector, was investigated. Thus, it can be assumed that the carbon signal from the glue did not contribute significantly to the carbon signal in the cross section evaluation since the electron beam was parallel to the substrate. Since the difference between the oxygen share in the top view and in the cross section is around 1 wt%, it can be concluded that the carbon glue does not play an important role in all EDX measurements, and the results are in good agreement with elemental analysis considering the addition of carbon black and binder. Figure S10 shows the EDX mapping of the cross section where the carbon is colored red, and copper is colored green and reveals the carbon is homogeneously distributed through the whole film.

From the physicochemical investigations of the spruce hard carbon, it can be concluded that the material has very similar properties compared to other biomass-derived hard carbons, except for the XPS measurement, which indicates a relatively high oxygen/carbon ratio. This relatively stronger surface oxidation can stem from the processing itself, especially with phosphoric acid, or from the subsequent storage of the material in an ambient atmosphere.

2.3. Half-Cell Tests

Half- and full-cell tests were performed to investigate the electrochemical performance of spruce hard carbon anode materials. Figure 4a shows the typical cyclic voltammogram of a spruce hard carbon-based half-cell. At low potentials and cathodic current, lithium ions are reversibly incorporated into
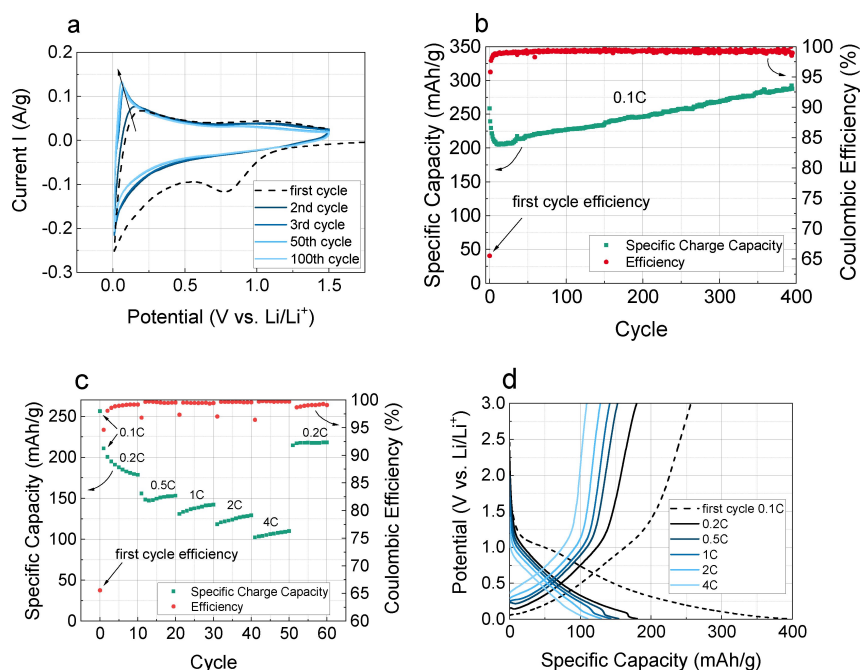

Figure 4. a) Cyclic voltammogram at a scan rate of 0.1 mV/s, b) long term cycling, c) rate capability test, and d) voltage profiles of spruce hard carbon anodes corresponding to c.

ChemElectroChem

Articles
doi.org/10.1002/celc.202101174

**Chemistry
Europe**
European Chemical
Societies Publishing

the hard carbon. On the anodic scan, there is a corresponding oxidation peak at around 0.2 V, suggesting reversible de-intercalation of lithium ions from the hard carbon matrix[21]. With increasing number of cycles, the signals shift to lower potentials (to around 0.05 V after 100 cycles) and the current increases. In former studies, the same trend was observed[21,23] and explained by the wetting of the anode and possible structural changes during charge and discharge processes.[23,29,46] In the first cathodic scan, there is a broad reduction signal at around 0.75 V, which can be associated with electrolyte decomposition and subsequent SEI formation.[19,21]

The long-term cycling of a spruce hard carbon-based half-cell are shown in Figure 4b. The cell shows an initial specific charge capacity higher than 250 mAh/g and a corresponding initial coulombic efficiency (CE) of approximately 65%. Such relatively low initial CEs are characteristic of hard carbon anodes[19,21,54] and represent one of the main challenges to be solved for industrially relevant LIBs. With further cycling, the capacity decreases to around 200 mAh/g, which is in accordance with many studies on biomass-based hard carbons.[19,23,53–57] Explanations from the literature regarding decreasing capacity head towards SEI formation, which is justified by an increasing SEI layer-related resistance analyzed by electrochemical impedance spectroscopy.[54,57] Although such conclusions seem reasonable and SEI formation is plausible because of the corresponding low coulombic efficiencies and an SEI-related signal in the Nyquist plot (high-frequency semi-circle), the impedance data collected here show a different trend (see supporting information and Figure S11b-c for the impedance spectroscopy study). In fact, except R_s from the pristine anode to the 5th cycle all real impedance contributions of the cell decrease from the pristine cell (R_s: 2.4 Ω, R_{ct}: 176.5 Ω) to the 5th cycle (R_s: 5.0 Ω, R_{SEI}: 8.3 Ω, R_{ct}: 15.2 Ω) and to the 20th cycle (R_s: 4.9 Ω, R_{SEI}: 8.0 Ω, R_{ct}: 12.8 Ω). Thus, possibly counter-acting processes lead to a decrease in the real total impedance despite SEI formation. Similar to our findings, Linsenmann et al. recently investigated the lithiation of hard carbon-based half-cells and found a decreasing capacity together with a decreasing cell resistance within the first two cycles.[58] Although the authors suggested the SEI formation as the reason for the decrease in capacity, they claimed "increasing surface area via opening of initially inaccessible pores leading to facilitated charge transfer"[58,59] as the reason for the decreasing impedance. Based on EIS data and literature review, we carefully suggest that the SEI formation and the transformation of the hard carbon material may be responsible for the experimental findings. Additionally, postmortem SEM and EDX results confirm the presence of an SEI layer (see supporting information and Figure S12 and S13). After this strong decrease during the first ten cycles, the capacity starts to increase after around 20 cycles and reached almost 300 mAh/g after 400 cycles. A similar cycling behavior for biomass-based hard carbons has been reported in the literature and explained by "activation processes",[23,60] although no further research is available to explain this increase in capacity. The impedance spectroscopy results presented here show continuously decreasing series (R_s), SEI layer (R_{SEI}), and charge transfer-related (R_{ct}) real impedances

over 60 cycles (see Figure S11d for detailed values). This might indicate an explanation for the increasing capacity, as the charge transfer processes seem to run more efficient with further cycles. As discussed for the decreasing capacity in the first few cycles, some of the underlying processes could indicate continuously improving accessibility of the electrolyte in pores and cavities. Similar conclusions were drawn by Campbell et al. for a Portobello mushroom-based hard carbon cell[23]. Finally, the CEs for the cell fabricated in this work reach 99% after the 10th cycle, and for subsequent cycles the CEs do not exceed 99.4%.

Figure 4c shows the rate capability of a spruce hard carbon anode. The initial specific charge capacity and CEs are comparable to the spruce hard carbon anode previously discussed (Figure 4b). With increasing charging rate, the capacity decreases, which is commonly accepted and due to kinetic limitations of the cell. For the initial cycling at 0.2 C, the capacity continuously decreases, which was also found for the corresponding long term cycling at 0.1 C (Figure 4b). At a current rate of 4 C, the cell showed capacity values of more than 100 mAh/g, which is close to values found for a sodium-ion battery with an apple-based hard carbon anode.[29] When the current rate returns to 0.2 C (after 50 cycles), the capacity of the cell significantly exceeds the values of the initial cycling at 0.2 C. Again, this can be explained by hypothesis stated for the long-term cycling.

Figure 4d shows typical voltage profiles of the hard carbon anode corresponding to the rate capability test. As already observed for cycling (Figure 4c), the specific charge capacities decrease with increasing C rate. Although no clear charge and discharge plateaus can be seen, it can be assumed that the ohmic drop and hence the internal resistances of the cell increase. Such effects would lead to decreased specific charge capacities. In the first cycle at a current rate of 0.1 C, where lithiation of the hard carbon material takes place, a broad signal was observed in the voltage range between 1.1 V and 0.5 V, which can be assigned to the SEI formation.[21] This is in good agreement with the behavior observed in cyclic voltammetry (see Figure 4a).

2.4. Full-Cell Tests

In order to use the spruce hard carbon anodes in a working lithium-ion full-cell, the challenge of low initial CEs needs to be overcome. Thus, a pretreatment based on electrochemical pre-lithiation was applied in a Swagelok® cell. Figure 5a shows the schematic representation of the pre-lithiation process and the full-cell operation. The charge and discharge profiles, the potential between counter electrode (spruce hard carbon) and the reference electrode (Li), are shown in Figure 5b. In the lithiation step, the cell reached a specific capacity of around 375 mAh/g. Although the cell type and current rate are different, similar specific capacities were observed in the half-cell measurement (Figure 4d). Again, a broad signal between 1.1 V and 0.5 V was observed, due to the SEI formation, indicating successful pre-lithiation. To make room for lithium originating
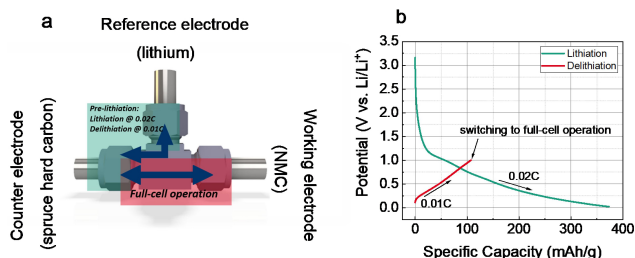
ChemElectroChem

Articles
doi.org/10.1002/celc.202101174

Chemistry Europe
European Chemical
Societies Publishing

Figure 5. Pre-lithiation method of spruce hard carbon anodes: a) schematic representation and b) corresponding charge and discharge curves (counter vs. reference electrode).

from the NMC cathode, the cell was subsequently charged to 1 V. A different battery chemistry, but the same pre-lithiation approach using the lithium reference of a three-electrode cell, was applied by Liu et al.[41] For hard carbon, a similar pretreatment was proposed by Rao et al.[61] However, the group used coin cells for pretreatment followed by transfer of the pre-lithiated anode to the full-cell, while the approach presented here allowed both steps in one assembly. The specific capacity of the de-lithiation step is relatively low (compared to half-cell measurements), which can be due to enhanced kinetic limitations, since the distance between reference electrode and spruce hard carbon anode was comparatively long and rectangularly aligned.

Figure 6a and b show the first cycle of the pre-lithiated and the pristine spruce hard carbon full-cell. Considering the mass loading (mAh/cm²) and the cycling rate of 0.1 C, specific capacities of 0.7–0.8 mAh/cm² were calculated for the spruce hard carbon anode. A capacity of 1.0 mAh/cm² was derived for

the cathode, considering a theoretical capacity of 145 mAh/g for NMC (111). The corresponding initial CE were 87% and 63%. The initial CE of the pristine spruce hard carbon anode cycled in the full-cell is in good agreement with that obtained in the half-cell measurements (Figure 4b–c), whereas the initial CE of the pre-lithiated spruce hard carbon anode was lower compared to the half-cell measurements. Here, an efficiency of approximately 95% was observed in the second cycle (compare Figure 4). The difference in internal CEs can be assigned to the formation of the cathode electrolyte interface. During the charge process, the anode terminated the cycle at 0.01 V when pre-lithiated. The corresponding potential of the cathode was 4.1 V, which is lower compared to its cut-off value of 4.3 V. Thus, it can be assumed that the anode is fully lithiated before the cathode is de-lithiated, which indicates an excess of lithium in the full-cell, either from the pre-lithiation process and/or from the oversized cathode. On discharge, the cathode reached its cut-off potential far earlier than the anode 3 V. Thus, the cathode was lithiated before the anode was fully de-lithiated, which again indicates an excess of lithium in the system. That the cathode is oversized supports the hypothesis that much of the excess lithium originates from the pre-lithiation process. If it came primarily from the oversized cathode, the anode should be fully de-lithiated before the cathode is lithiated. In cases where only the full-cell potential is controllable (in a two-electrode setup), such a lithiation state would lead to lithium plating on the anode[62]. Thus, with respect to more industrial cell configurations (e.g., pouch or prismatic cells), a more suitable pre-lithiation method/step would be required.[38]

For the pristine anode-based full-cell, higher capacities can be observed in the first lithiation step, including the characteristic anodic signal between 1.1 V and 0.5 V. Thus, significant SEI
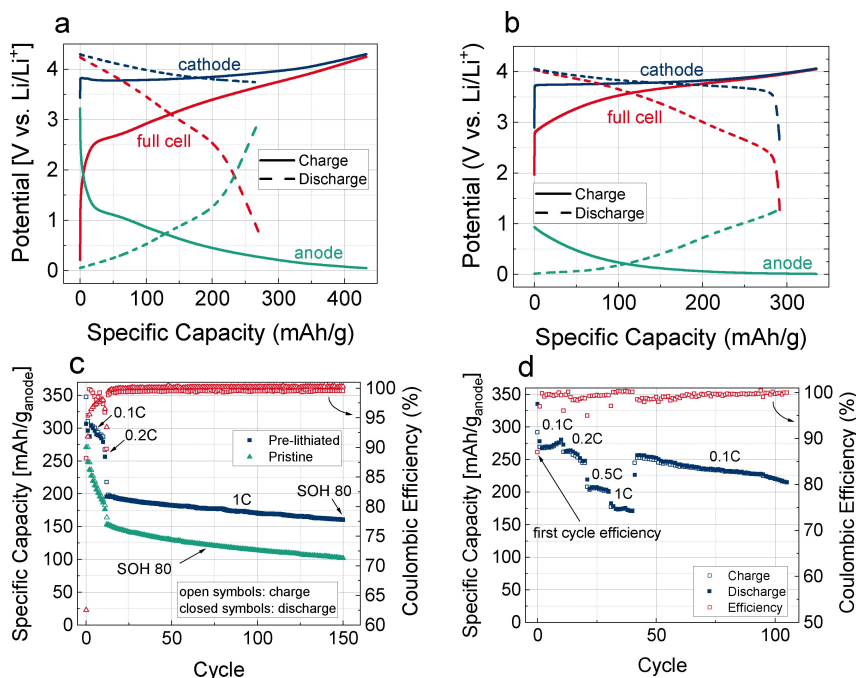

Figure 6. First cycle of a) pristine and b) pre-lithiated spruce hard carbon-based full-cell at a current rate of 0.05 C, c) long-term cycling of a pristine and pre-lithiated and d) rate capability of a pre-lithiated spruce hard carbon-based full-cell.

ChemElectroChem

Articles
doi.org/10.1002/celc.202101174

Chemistry Europe
European Chemical
Societies Publishing

formation is likely the cause for the low initial CE. In contrast to Figure 6a, the anode was cycled in nearly the full voltage range between 0.05 V and 3 V. Since the cathode was charged up to 4.3 V and subsequently discharged to only 3.75 V, it can be assumed that a significant amount of lithium was consumed for the SEI formation within the first cycle. A detailed discussion of the potential evolution in dependence of the cycle can be found at the end of this section.

Figure 6c shows the long-term cycling of the pristine and the pre-lithiated spruce hard carbon anode full-cell. For the pristine anode, the cell initially discharged to approximately 275 mAh/g. On subsequent cycling at a current of 0.1 C, the capacity decreased dramatically and reached 175 mAh/g after 10 cycles. The great losses again indicate an enormous lithium consumption within the first cycles. In addition, the capacity decay can also be due to structural changes in the anode, as already discussed in the half-cell section. At a current rate of 1 C, the pristine spruce hard carbon anode full-cell had a specific charge capacity of about 150 mAh/g and the subsequent capacity losses decelerated (in comparison with cycling at 0.1 C). After 8 charging and discharging cycles, the CE reached 99.9%. However, the capacity decreased continuously, and the pristine spruce hard carbon anode full-cell had a capacity retention of 80% (SOH80, referring to initial capacity at 1 C) after 70 cycles. For the pre-lithiated spruce hard carbon anode full-cell, the specific charge capacity was significantly increased and reached approximately 300 mAh/g at a current rate of 0.1 C. Relatively high capacity losses were observed within the first 10 cycles. However, the capacity losses were much lower compared to the pristine anode. At a current rate of 1 C, the specific charge capacity decreased to 195 mAh/g and CEs of 99.5% were reached for further cycling. Similar to the full-cell containing the pristine anode, the specific charge capacities stabilized, and the cell reached SOH80 after 150 cycles. Recently, Nowak et al. published the investigation results of lignin-based carbon fibers as anodes for lithium-ion full-cells. The lignin had been extracted from spruce and pine, but in a more expensive way compared to our work. Lithium-ion full-cells containing LFP cathodes and lignin carbon fiber anodes showed capacities of around 100 mAh/g and a capacity retention of 97% after 22 cycles at 0.1 C cycling.[34] Thus, the spruce hard carbon presented here is characterized not only by a simpler synthesis but also by improved full-cell performance. A study on pre-lithiated lithium-ion full-cells using tire waste-derived hard carbon was published by Gnanaraj et al.[32] The pre-lithiation was based on direct contact between lithium and the hard carbon anode, and the pouch full-cell showed a capacity retention of almost 99% after 60 cycles (0.2 C). However, the operation of the full-cell, including the pre-lithiation state during cycling, was not discussed in detail. Although the group presented almost 200 full-cell cycles, a corresponding state of health was hard to define since current rates and voltage ranges differed during cycling. Table S4 in the supporting information summarizes selected lithium-ion full-cells, one being bio/waste-based hard carbon anodes and the other being commercial hard carbon anodes.

Figure 6d shows the rate capability of a pre-lithiated spruce hard carbon anode full-cell. The observed specific capacities are in good agreement with the long-term cycling experiment. However, a high specific capacity reduction was observed from cycling at 0.1 C to 1 C. After returning to the current rate of 0.1 C, the cell showed a capacity retention of 92% (referred to initial cycling at 0.1 C). This is in accordance with the long-term cycling and suggests minor influences on the cell during moderate charging. Wu et al. showed similar cycling results for sodium-ion batteries based on apple waste, but with better rate performance.[29]

Figure 7a shows the anode, cathode, and full-cell voltage profile of the 2nd, 25th, 75th, 100th, and 150th cycles of a pre-lithiated spruce hard carbon anode full-cell (corresponding voltage profiles of a non-pre-lithiated full-cell are shown in supplementary information Figure S14). The first two cycles have similar voltage profiles and cut-off values (see Figure 6b), suggesting that some amount of extra lithium is still present in the cell. With increasing cycles, the anode and cathode discharge potentials reached values of 3 V and approximately 3.6 V, respectively. The corresponding rate capability test (see Figure 7b) showed the same trend.

To analyze the full-cell operation and particularly the lithiation state of the cell, the potential evolution of the anode, cathode and full-cell depending on the number of cycles for the pre-lithiated and the non-lithiated spruce hard carbon anode full-cells are shown in Figure 7c and d, respectively. A similar analysis was already proposed by Song et al. for a pre-lithiated silicon composite anode.[62] For the pre-lithiated spruce hard carbon anode full-cell (Figure 7c), it was observed that the charge potentials of the anode, cathode, and full-cell were almost steady, with the anode stopping each charge step at 0.01 V. The corresponding cathode and full-cell potentials were 4.11 V and 4.10 V. When the current rate increased, it was observed that the cathode and full-cell potentials decreased to 4.03 V and 4.02 V. The overall evolution of the charge potentials suggests that there is a specific amount of extra lithium in the cell over 150 cycles since the cathode is never fully de-lithiated (to 4.30 V). The discharge potentials showed a greater variation. For the first 4 cycles, the cathode was the first to reach the cut-off potential of 2.50 V. Thus, it can be stated that there is enough excess lithium in the system to fully lithiate the cathode although the anode is not fully de-lithiated. In the meantime, the cut-off voltage of the anode increased, suggesting consumption of lithium due to SEI formation. However, before the anode potential was at 3.00 V, the full-cell reached its cut-off value of 0 V. Finally, the anode reached the cut-off potential of 3.00 V after 10 cycles. From this cycle on, the anode was charged and discharged in its full operation range between 0.01 V and 3.00 V, suggesting the full consumption of lithium from the pre-lithiation process. Around the 10th cycle, an abrupt increase of the full-cell potential and a decrease in the cathode and anode potentials were observed, which was likely due to the increased current rate (from 0.1 C to 0.2 C and to 1 C) and corresponding kinetic effects. For the subsequent cycle, the cathode and full-cell discharge potentials increased continuously and reached values of 3.6 V and 0.6 V, respectively. This
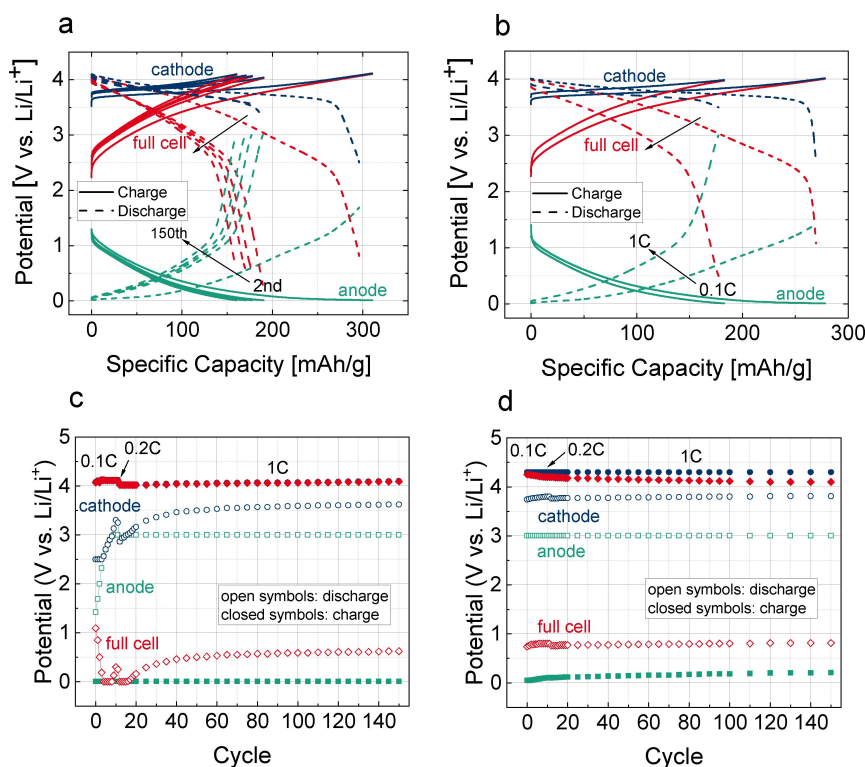
Figure 7. Voltage profile of a) the 2nd, 25th, 75th, 100th, and 150th cycles and of b) charging cycles at 0.1 C and 1 C of a pre-lithiated spruce hard carbon anode full-cell. Anode, cathode, and full-cell potential of c) a pre-lithiated and d) a pristine spruce hard carbon anode full-cell.

trend corresponds to further lithium-ion losses, since the cathode cannot be fully lithiated although the anode is already fully de-lithiated. The reason why the cathode reached a steady value of 4.03 V in the charge step is likely due to the fact that the capacity of the cathode was initially oversized compared to the anode. Therefore, the lithium originating from the cathode cannot be intercalated in the anode even after 150 cycles. For the pristine spruce hard carbon anode full-cell, it can be observed that the charge and discharge voltage values were quite steady. From the first cycle, the cathode was charged to 4.3 V and subsequently discharged to only 3.75 V, suggesting that the cathode can be fully de-lithiated but not fully lithiated again. Thus, it can be assumed that a significant part of the lithium is consumed by the SEI formation during the first cycle. The fact that the anode was simultaneously operating in its almost full voltage range (between 0.05 V and 0.21 V–3 V) is due to the oversized capacity of the cathode. With increasing cycles, the potential of the anode increased slightly, reaching 0.21 V after 150 cycles. The increase suggests further lithium-ion losses since the anode cannot be fully lithiated. With this understanding of the lithiation state of the pre-lithiated full-cell, the pre-lithiation process should be optimized in order to exclude cell damage by, e.g., lithium plating in industrial relevant two-electrode LIBs.

3. Conclusions

In this work, we presented the pyrolysis of spruce raw material to produce hard carbon anode material . Based on this material, we succeeded in developing a lithium-ion full-cell with enhanced cycle life using electrochemical pre-lithiation. By various characterization techniques, including elemental analysis, X-ray diffraction, Raman spectroscopy, energy dispersive X-ray spectroscopy, X-ray photoelectron spectroscopy, physisorption measurements and scanning and high-resolution transmission electron microscopy, composition, microstructure, and morphological features typical for hard carbons were found.

Thus, spruce hard carbon consists of sp^2 and sp^3-hybridized carbon atoms and shows a significant amount of surface functionalization. Pore sizes range from micro- to mesopores, with determining share of micro- and larger mesopores, and a BET surface area of 61 m^2/g was found. Half-cell measurements showed specific charge capacities of 225 mAh/g at a current rate of 0.1 C and 110 mAh/g at 4 C. However, the low initial coulombic efficiency of 65% reflect the major challenge of hard carbon anodes for full-cell operation. To overcome this hurdle for full-cell operation, electrochemical pre-lithiation was conducted in-situ in a Swagelok® cell. In this setup, the reference electrode was used to initially lithiate the anode at a current rate of 0.02 C and subsequently de-lithiate the anode at 0.01 C to 1 V. As a result, pre-lithiated spruce hard carbon anode full-cells (with NMC cathodes) exhibited an initial coulombic efficiency of 87% and a specific charge capacity of 195 mAh/g

ChemElectroChem

Articles
doi.org/10.1002/celc.202101174

**Chemistry
Europe**
European Chemical
Societies Publishing

at a current rate of 1 C. After 150 cycles, the full-cell showed a capacity retention of 80% (SOH 80). In comparison, the non-lithiated spruce hard carbon anode full-cell had significantly lower capacities, an initial coulombic efficiency of 63% and a capacity retention of only 66% after 150 cycles. To investigate the full-cell operation with respect to the pre-lithiation state in more detail, the potential evolution of the anode, cathode and full-cell was studied. It was shown that the extra lithium from the pre-lithiated anode was consumed after 10 cycles. In contrast, in the pristine spruce hard carbon anode full-cell, a significant part of the lithium derived from the cathode was consumed within the SEI formation of the first cycle.

In summary, this work demonstrates functional lithium-ion full-cells using biomass-derived hard carbon anodes in combination with an in-situ electrochemical pre-lithiation process. With its comparably high capacity, rate capability and capacity retention, spruce hard carbon is a promising candidate to replace conventional graphite in lithium-ion battery anodes. However, it must be noted that the full-cells have capacities and a capacity decay that do not yet meet industrial standards. Thus, further research on synthesis is needed to adjust the physicochemical properties, which would lead to improved electrochemical performance. Furthermore, the pre-lithiation process presented in this work is not applicable for large-scale manufacturing. Therefore, a process for pre-lithiation has to be developed with respect to more efficient battery operation and industrial applicability.

Experimental

Material Synthesis

Pieces of spruce wood were collected in the Black Forest and dried for 1 month at ambient conditions. After drying, the pieces were shredded with an electric jigsaw (Makita, DJV181RT1 J, Japan) to obtain sawdust. The sawdust was dried at 80°C for 72 h before being dispersed in phosphoric acid as described in.[29] After resting for 6 days, the dispersion was rinsed with deionized water until a pH value close to 7 was reached. Then the dispersion was decanted, and the sawdust was dried at 100°C for 72 hours. 14 g of sawdust were pyrolyzed in a beaker under nitrogen atmosphere at 1100°C for 6 hours (Nabertherm, N7H, Germany). After pyrolysis, 6 g of spruce hard carbon were obtained. To obtain smaller particle sizes, the product was ball milled at 500 rpm for 3 hours with 2 mm zirconium oxide balls (Retsch, PM100, Germany). Subsequently, the spruce hard carbon powder was sifted using a sieve (VWR group, Germany) with a mesh size of 53 μm. Only the fraction with particle sizes of below 53 μm was used for electrochemical and physicochemical characterization.

Electrode Preparation and Cell Assembly

For the spruce hard carbon slurries, carboxymethylcellulose (CMC, Merck group) was suspended in deionized water by magnetic stirring for 1 hour. When the dispersion was fully homogenized, styrene-butadiene rubber dispersion (SBR, 85 wt% H_2O, Targray group) was added at a weight ratio of 1:1. After stirring for another 30 minutes, spruce hard carbon and carbon black (100% compressed, 99.9%, Alfa Aesar) were added. The weight fractions of spruce hard carbon, carbon black and binder (CMC and SBR) were

80 wt%, 10 wt% and 10 wt%. Subsequently, the slurry was homogenized at 3500 rpm for 2 minutes (DAC 150/250, Speedmixer, Germany). To further homogenize the slurry and adjust the particle sizes, a three-roll mill (80E, Exakt Advanced Technologies, Germany) with a small and a wide roll distance of 10 and 20 μm was applied. Finally, the slurry was coated on copper foils with a wet film thickness of 100 μm. After pre-drying the coating at 40°C for 24 hours, coins of 12 and 14 mm were cut and then vacuum dried together with the NMC cathodes at 120°C for 12 hours.

Physicochemical Characterization

X-ray diffraction patterns of spruce hard carbon powders were collected using a Miniflex 600 (Rigaku, Japan) with a copper source ($\lambda = 1.54$ Å), a step width of 0.02°, and speed of 0.1°/min operating at 40 kV and 15 mA. Raman measurements were conducted on an Alpha500 confocal Raman microscope (WITec, Germany) with a laser wavelength of 532 nm and a power of 50 mW. Surface area and the nitrogen adsorption–desorption isotherms were determined by nitrogen adsorption at 77 K in a QuadraSorb Station 3 (Quantachrome Instruments, US) instrument using a quenched solid density functional theory (QSDFT adsorption branch) model. Elemental analysis (CHNS, carbon, hydrogen, nitrogen, sulfur) was performed in a vario MICRO cube (elementar, Germany). The microstructure, morphology, film thickness and elemental composition of the as synthesized hard carbon powder and the as prepared coin electrodes were characterized by electron microscopy (HR-SEM, Hitachi SU8220, acceleration voltage 5 kV) and energy dispersive X-ray spectroscopy (EDX, Bruker XFlash 6130, excitation with an electron beam with an acceleration voltage of 5 kV). Therefore, the hard carbon samples (powder and electrode) were mounted on a carbon-containing copper adhesive tape. High-resolution transmission electron microscopy (HRTEM) was conducted using a spherical aberration (Cs) image corrected Thermo Scientific Titan Themis 60–300 instrument at an acceleration voltage of 300 kV. The elemental surface composition of the as synthesized hard carbon powder was characterized by X-ray photoelectron spectroscopy (XPS, Phi 5600 Perkin Elmer with Mg Kα-radiation). The pass energy for the survey spectrum was 187.5 eV and for the detailed spectra 23.5 eV.

Electrochemical Characterization

Spruce hard carbon anodes were investigated in half-cell and full-cell configurations. Cell assembly was performed in an argon-filled glovebox (E-Line, GS Glovebox System, Germany, $O_2 < 3$ ppm, $H_2O < 0.5$ ppm). Half-cells were assembled using CR2032 coin cell casings, a glass fiber separator (Whatman, GF/A, thickness 1 mm), and 300 μL of LP30 (1 M $LiPF_6$ in ethylene carbonate (EC) and dimethyl carbonate (DMC) 1:1 (by vol%), battery grade, Merck group). Lithium metal was used as counter electrode. For full-cell measurements, Swagelok® cells and a commercial cathode with $Li[Ni_{0.33}Mn_{0.33}Co_{0.33}O_2]$ (NMC (111), Custom Cells, Germany) as active material were used. A spruce hard carbon anode was used as counter electrode and lithium metal as the reference electrode. A PVDF membrane (Durapore®, 0.22 μm pore size, thickness 125 μm, Merck group) was used as a separator soaked with 120 μL of LP30. The mass loading of the anode ranged from 3.01 mg/cm² and 3.09 mg/cm². Values of approximately 7.07 mg/cm² were found for the cathode.

Electrochemical tests for half-cells were performed on a BCS-805 (BioLogic, France) battery tester in the voltage range between 0.01 V and 3 V vs. Li/Li⁺. The formation cycle of all cells was done at a current rate of 0.05 C. For subsequent tests, cells were cycled either in constant current (CC) mode at a current rate of 0.1 C or for

ChemElectroChem

Articles
doi.org/10.1002/celc.202101174

Chemistry Europe
European Chemical
Societies Publishing

rate capability (CC) tests at 0.1 C, 0.2 C, 0.5 C, 1 C, 2 °C and 4 C, for 10 cycles with 10 min rest after each charge and discharge step. Electrochemical impedance spectroscopy data in dependence on the cycle number were collected in the de-lithiated state (3 V vs. Li/Li$^+$) after 2 hours of relaxation. The frequency range was set from 10 kHz to 1 Hz with a voltage amplitude of 10 mV. Cyclic voltammetry was performed in the voltage range between 0.01 V and 1.5 V with a scan rate of 0.1 mV/s. Full-cell experiments were conducted with a VMP3 potentiostat (BioLogic, France). The voltage ranges for anode, cathode, and full-cell were 0.01–3 V, 2.5–4.3 V and 0–4.3 V. The current cycle was stopped if one of the limits was exceeded. The formation of the cells included a charge and discharge cycle at 0.05 C. For long-term stability measurements, cells were cycled in CC mode at a current rate of 0.1 C for 10 cycles and at 1 C until the cell reached a state of health (SOH) value of 80%, with a 10 min rest after each charge and discharge step. Cycling for rate capability tests was performed at 0.1 C, 0.2 C, 0.5 C and 1 C. Pre-lithiation of the spruce hard carbon anodes was done by applying a current rate of 0.02 C between the anode and reference electrode down to 0.02 V for lithiation and a current rate of 0.01 C up to 1 V for de-lithiation.

Acknowledgements

Conflict of Interest

The authors declare no conflict of interest.

[1] E. A. Olivetti, G. Ceder, G. G. Gaustad, X. Fu, *Joule* **2017**, *1*, 22.
[2] S. Dühnen, J. Betz, M. Kolek, R. Schmuch, M. Winter, T. Placke, *Small Methods* **2020**, *4*, 2000039.
[3] a) "Report on Critical Raw Materials and the Circular Economy", can be found under https://ec.europa.eu/docsroom/documents/27348/attachements/1/translations/en/renditions/pdf;; b) "U.S. Department of the Interior, U.S. Geological Survey, Draft Critical Mineral List", can be found under https://pubs.usgs.gov/of/2018/1021/ofr20181021.pdf.
[4] "In your phone, in the air. A trace of graphite is in consumer tech. In these Chinese villages, it's everywhere.", can be found under https://www.washingtonpost.com/graphics/business/batteries/graphite-mining-pollution-in-china/.
[5] "Ökologische und sozio-ökonomische Herausforderungen in Batterie Lieferketten: Graphit und Lithium", can be found under https://www.oeko.de/fileadmin/oekodoc/Graphit-Lithium-Oeko-Soz-Herausforderungen.pdf.
[6] B. N. Loeffler, D. Bresser, S. Passerini, M. Copley, *Johnson Matthey Technol. Rev.* **2015**, *59*, 34.
[7] E. R. Buiel, A. E. George, J. R. Dahn, *Carbon* **1999**, *37*, 1399.
[8] W. Xing, J. R. Dahn, *J. Electrochem. Soc.* **1997**, *144*, 1195.
[9] W. Xing, J. S. Xue, J. R. Dahn, *J. Electrochem. Soc.* **1996**, *143*, 3046.
[10] W. E. Tenhaeff, O. Rios, K. More, M. A. McGuire, *Adv. Funct. Mater.* **2014**, *24*, 86.
[11] D. A. Stevens, J. R. Dahn, *J. Electrochem. Soc.* **2000**, *147*, 1271.
[12] a) B.-H. Hou, Y.-Y. Wang, Q.-L. Ning, W.-H. Li, X.-T. Xi, X. Yang, H.-J. Liang, X. Feng, X.-L. Wu, *Advanced materials (Deerfield Beach, Fla.)* **2019**, *31*, e1903125; b) J. Ding, H. Wang, Z. Li, A. Kohandehghan, K. Cui, Z. Xu, B. Zahiri, X. Tan, E. M. Lotfabad, B. C. Olsen et al., *ACS Nano* **2013**, *7*, 11004.
[13] S. Qiu, L. Xiao, M. L. Sushko, K. S. Han, Y. Shao, M. Yan, X. Liang, L. Mai, J. Feng, Y. Cao et al., *Adv. Energy Mater.* **2017**, *7*, 1700403.
[14] Z. Wang, X. Feng, Y. Bai, H. Yang, R. Dong, X. Wang, H. Xu, Q. Wang, H. Li, H. Gao et al., *Adv. Energy Mater.* **2021**, *11*, 2003854.
[15] X. Zhang, H. Qu, W. Ji, D. Zheng, T. Ding, C. Abegglen, D. Qiu, D. Qu, *ACS Appl. Mater. Interfaces* **2020**, *12*, 11589.
[16] X. Liao, J. Yu, L. Gao, *J. Solid State Electrochem.* **2012**, *16*, 423.
[17] T. Zhang, J. Mao, X. Liu, M. Xuan, K. Bi, X. L. Zhang, J. Hu, J. Fan, S. Chen, G. Shao, *RSC Adv.* **2017**, *7*, 41504.
[18] Y. Zhu, Y. Huang, C. Chen, M. Wang, P. Liu, *Electrochim. Acta* **2019**, *321*, 134698.
[19] Y. Zhang, Y. Wang, Y. Meng, G. Tan, Y. Guo, D. Xiao, *RSC Adv.* **2016**, *6*, 98434.
[20] a) G. T.-K. Fey, Y.-D. Cho, C.-L. Chen, Y.-Y. Lin, T. P. Kumar, S.-H. Chan, *Pure Appl. Chem.* **2010**, *82*, 2157; b) D. S. Jung, M.-H. Ryou, Y. J. Sung, S. B. Park, J. W. Choi, *PNAS* **2013**, *110*, 12229.
[21] Y. Li, Y. Huang, K. Song, X. Wang, K. Yu, C. Liang, *ChemistrySelect* **2019**, *4*, 4178.
[22] U. Kumar, J. Wu, N. Sharma, V. Sahajwalla, *Energy Fuels* **2021**, *35*, 1820.
[23] B. Campbell, R. Ionescu, Z. Favors, C. S. Ozkan, M. Ozkan, *Sci. Rep.* **2015**, *5*, 14575.
[24] a) T. Lyu, X. Lan, L. Liang, X. Lin, C. Hao, Z. Pan, Z. Q. Tian, P. K. Shen, *Electrochim. Acta* **2021**, *365*, 137356; b) J. Tang, V. Etacheri, V. G. Pol, *ACS Sustainable Chem. Eng.* **2016**, *4*, 2624.
[25] E. M. Lotfabad, J. Ding, K. Cui, A. Kohandehghan, W. P. Kalisvaart, M. Hazelton, D. Mitlin, *ACS Nano* **2014**, *8*, 7115.
[26] P. Liu, Y. Li, Y.-S. Hu, H. Li, L. Chen, X. Huang, *J. Mater. Chem.* **2016**, *4*, 13046.
[27] J. Xiang, W. Lv, C. Mu, J. Zhao, B. Wang, *J. Alloys Compd.* **2017**, *701*, 870.
[28] T. J. Yokokura, J. R. Rodriguez, V. G. Pol, *ACS Omega* **2020**, *5*, 19715.
[29] L. Wu, D. Buchholz, C. Vaalma, G. A. Giffin, S. Passerini, *ChemElectroChem* **2016**, *3*, 292–298.
[30] K. Yu, H. Zhao, X. Wang, M. Zhang, R. Dong, Y. Li, Y. Bai, H. Xu, C. Wu, *ACS Appl. Mater. Interfaces* **2020**, *12*, 10544.
[31] Y. Wang, Y. Li, S. S. Mao, D. Ye, W. Liu, R. Guo, Z. Feng, J. Kong, J. Xie, *Sustain. Energy Fuels* **2019**, *3*, 717.
[32] J. Gnanaraj, R. Lee, A. Levine, J. Wistrom, S. Wistrom, Y. Li, J. Li, K. Akato, A. Naskar, M. Paranthaman, *Sustainability* **2018**, *10*, 2840.
[33] T. Qiu, J.-G. Yang, X.-J. Bai, Y.-L. Wang, *RSC Adv.* **2019**, *9*, 12737.
[34] A. P. Nowak, J. Hagberg, S. Leijonmarck, H. Schweinebarth, D. Baker, A. Uhlin, P. Tomani, G. Lindbergh, *Holzforschung* **2018**, *72*, 81.
[35] I. Elizabeth, B. P. Singh, S. Trikha, S. Gopukumar, *J. Power Sources* **2016**, *329*, 412.
[36] J. Ou, Y. Zhang, L. Chen, Q. Zhao, Y. Meng, Y. Guo, D. Xiao, *J. Mater. Chem.* **2015**, *3*, 6534.
[37] J. Ou, Y. Zhang, L. Chen, H. Yuan, D. Xiao, *RSC Adv.* **2014**, *4*, 63784.
[38] F. Holtstiege, P. Bärmann, R. Nölle, M. Winter, T. Placke, *Batteries* **2018**, *4*, 4.
[39] A. Shellikeri, V. G. Watson, D. L. Adams, E. E. Kalu, J. A. Read, T. R. Jow, J. P. Zheng, *ECS Trans.* **2017**, *77*, 293.
[40] T. Watanabe, T. Tsuda, N. Ando, S. Nakamura, N. Hayashi, N. Soma, T. Gunji, T. Ohsaka, F. Matsumoto, *Electrochim. Acta* **2019**, *324*, 134848.
[41] C. Liu, N. Kim, G. W. Rubloff, S. B. Lee, *Nanoscale* **2017**, *9*, 11566.
[42] a) Y. Shen, J. Qian, H. Yang, F. Zhong, X. Ai, *Small* **2020**, *16*, e1907602; b) G. Wang, F. Li, D. Liu, D. Zheng, Y. Luo, D. Qu, T. Ding, D. Qu, *ACS Appl. Mater. Interfaces* **2019**, *11*, 8699.
[43] a) M. W. Forney, M. J. Ganter, J. W. Staub, R. D. Ridgley, B. J. Landi, *Nano Lett.* **2013**, *13*, 4158; b) B. Xiao, F. A. Soto, M. Gu, K. S. Han, J. Song, H. Wang, M. H. Engelhard, V. Murugesan, K. T. Mueller, D. Reed et al., *Adv. Energy Mater.* **2018**, *8*, 1801441; c) C. R. Jarvis, M. J. Lain, M. V. Yakovleva, Y. Gao, *J. Power Sources* **2006**, *162*, 800.
[44] S.-F. Huang, Y. Lv, Da Tie, Y. Yu, Y.-F. Zhao, *Rare Met.* **2021**, *40*, 1.
[45] X. Dou, C. Geng, D. Buchholz, S. Passerini, *APL Mater.* **2018**, *6*, 47501.
[46] X. Dou, I. Hasa, M. Hekmatfar, T. Diemant, R. J. Behm, D. Buchholz, S. Passerini, *ChemSusChem* **2017**, *10*, 2668.
[47] K. Hong, L. Qie, R. Zeng, Z. Yi, W. Zhang, D. Wang, W. Yin, C. Wu, Q. Fan, W. Zhang et al., *J. Mater. Chem.* **2014**, *2*, 12733.
[48] K. Wang, Y. Jin, S. Sun, Y. Huang, J. Peng, J. Luo, Q. Zhang, Y. Qiu, C. Fang, J. Han, *ACS Omega* **2017**, *2*, 1687.
[49] Q. Zhang, X. Deng, M. Ji, Y. Li, Z. Shi, *Ionics* **2020**, *26*, 4523.
[50] C. Matei Ghimbeu, B. Zhang, A. Martinez de Yuso, B. Réty, J.-M. Tarascon, *Carbon* **2019**, *153*, 634.

ChemElectroChem

Articles
doi.org/10.1002/celc.202101174

Chemistry Europe
European Chemical
Societies Publishing

[51] A. Sadezky, H. Muckenhuber, H. Grothe, R. Niessner, U. Pöschl, *Carbon* **2005**, *43*, 1731.

[52] a) J. Melke, J. Martin, M. Bruns, P. Hügenell, A. Schökel, S. Montoya Isaza, F. Fink, P. Elsässer, A. Fischer, *ACS Appl. Energ. Mater.* **2020**, *3*, 11627; b) H. Wang, F. Sun, Z. Qu, K. Wang, L. Wang, X. Pi, J. Gao, G. Zhao, *ACS Sustainable Chem. Eng.* **2019**, *7*, 18554; c) K. Kaare, E. Yu, A. Volperts, G. Dobele, A. Zhurinsh, A. Dyck, G. Niaura, L. Tamasauskaite-Tamasiunaite, E. Norkus, M. Andrulevičius et al., *ACS Omega* **2020**, *5*, 23578.

[53] S. Alijani, S. Capelli, S. Cattaneo, M. Schiavoni, C. Evangelisti, K. M. H. Mohammed, P. P. Wells, F. Tessore, A. Villa, *Catalysts* **2020**, *10*, 11.

[54] H. Wang, W. Yu, J. Shi, N. Mao, S. Chen, W. Liu, *Electrochim. Acta* **2016**, *188*, 103.

[55] C. J. Jafta, X.-G. Sun, H. Lyu, H. Chen, B. P. Thapaliya, W. T. Heller, M. J. Cuneo, R. T. Mayes, M. P. Paranthaman, S. Dai et al., *Adv. Funct. Mater.* **2021**, *31*, 2008708.

[56] C. Chen, Z. Wang, B. Zhang, L. Miao, J. Cai, L. Peng, Y. Huang, J. Jiang, Y. Huang, L. Zhang et al., *Energy Storage Mater.* **2017**, *8*, 161.

[57] K. Tang, L. Fu, R. J. White, L. Yu, M.-M. Titirici, M. Antonietti, J. Maier, *Adv. Energy Mater.* **2012**, *2*, 873.

[58] F. Linsenmann, D. Pritzl, H. A. Gasteiger, *J. Electrochem. Soc.* **2021**, *168*, 10506.

[59] F. Linsenmann, D. Pritzl, H. A. Gasteiger, *J. Electrochem. Soc.* **2019**, *166*, A3668–A3674.

[60] a) L. Qie, W.-M. Chen, Z.-H. Wang, Q.-G. Shao, X. Li, L.-X. Yuan, X.-L. Hu, W. Zhang, Y. Huang, *Advanced materials (Deerfield Beach, Fla.)* **2012**, *24*, 2047; b) K. Xu, Y. Li, J. Xiong, X. Ou, W. Su, G. Zhong, C. Yang, *Front. Chem.* **2018**, *6*, 366.

[61] X. Rao, Y. Lou, J. Chen, H. Lu, B. Cheng, W. Wang, H. Fang, H. Li, S. Zhong, *Front. Energy Res.* **2020**, *8*.

[62] B. F. Song, A. Dhanabalan, S. L. Biswal, *J. Energy Storage* **2020**, *28*, 101268.